

Prospects for clustering and lensing measurements with forthcoming intensity mapping and optical surveys

A. Pourtsidou¹, D. Bacon¹, R. Crittenden¹, R. B. Metcalf²

¹ *Institute of Cosmology & Gravitation, University of Portsmouth, Burnaby Road, Portsmouth, PO1 3FX, United Kingdom*

² *Dipartimento di Fisica e Astronomia, Alma Mater Studiorum Università di Bologna, viale Berti Pichat, 6/2, I-40127, Bologna, Italy*

8 May 2022

ABSTRACT

We explore the potential of using intensity mapping surveys (MeerKAT, SKA) and optical galaxy surveys (DES, LSST) to detect HI clustering and weak gravitational lensing of 21cm emission in auto- and cross-correlation. Our forecasts show that high precision measurements of the clustering and lensing signals can be made in the near future using the intensity mapping technique. Such studies can be used to test the intensity mapping method, and constrain parameters such as the HI density Ω_{HI} , the HI bias b_{HI} and the galaxy-HI correlation coefficient $r_{\text{HI-g}}$.

Key words: cosmology: theory — observations — large-scale structure of the universe — gravitational lensing: weak

1 INTRODUCTION

Intensity mapping (Battye et al. 2004; Chang et al. 2008; Loeb & Wyithe 2008; Mao et al. 2008; Peterson et al. 2009; Seo et al. 2010; Ansari et al. 2012; Battye et al. 2013; Switzer et al. 2013; Bull et al. 2015) is an innovative technique which uses neutral hydrogen (HI) to map the large-scale structure of the Universe in three dimensions. Instead of detecting individual galaxies like the conventional galaxy surveys, intensity mapping surveys use HI as a dark matter tracer by measuring the intensity of the redshifted 21cm line across the sky and along redshift, treating the 21cm sky as a diffuse background, similar to the Cosmic Microwave Background (CMB).

Santos et al. (2015) investigated the potential of the planned Square Kilometre Array¹ (SKA) to deliver HI intensity mapping maps over a broad range of frequencies and a substantial fraction of the sky. Detecting the 21cm signal in auto- and cross-correlation using intensity mapping and optical galaxy surveys is essential in order to exploit the intensity mapping technique, test foreground removal methods and identify and control systematic effects. This is possible using SKA pathfinders like MeerKAT² and, as we will show, in many cases high signal-to-noise measurements can be achieved.

Cross-correlation between large scale structure (LSS) traced by galaxies and 21-cm intensity maps at $z \sim 1$ was first detected using the Green Bank Telescope (GBT) and the DEEP2 optical galaxy redshift survey (Chang et al.

2010); this measurement was improved using the GBT and the WiggleZ Dark Energy Survey (Masui et al. 2013). The auto-power spectrum of 21 cm intensity fluctuations using data acquired with the GBT was used in Switzer et al. (2013) to constrain HI fluctuations at $z \sim 0.8$ and was interpreted as an upper bound on the 21cm signal because of residual foreground contamination bias.

In this work we present HI detection forecasts for auto- and cross-correlation measurements using intensity mapping surveys with MeerKAT and SKA, and optical galaxy surveys with the Dark Energy Survey (DES)³ and the Large Synoptic Survey Telescope (LSST)⁴. Our forecasts concern both the HI intensity fluctuations as well as the weak gravitational lensing of 21-cm emission, using the weak lensing intensity mapping method developed in Pourtsidou & Metcalf (2014, 2015). In the following we denote the density fluctuations δ using the subscript HI for 21-cm and g for galaxies. We also denote the lensing convergence κ using the subscript g when it is detected using galaxies and IM when using the intensity mapping method.

In Section 2 we introduce the HI intensity mapping and optical galaxy surveys we are going to use for our clustering and lensing measurements forecasts and analyse their noise properties. In Section 3 we study correlations of the HI observables. We investigate the possibility of measuring the HI-HI power spectrum ($\delta_{\text{HI}} \times \delta_{\text{HI}}$) with MeerKAT and show forecasts for the lensing convergence power spectrum measurements ($\kappa_{\text{IM}} \times \kappa_{\text{IM}}$) and for $\delta_{\text{HI}} \times \kappa_{\text{IM}}$ using

¹ www.skatelescope.org

² <http://www.ska.ac.za/meerkat/>

³ <http://www.darkenergysurvey.org/>

⁴ <http://www.lsst.org/>

MeerKAT/SKA Phase 1 (SKA1) and the intensity mapping method. Cross-correlation studies are less susceptible to systematic contamination than auto-correlations, and can be observed when the noise levels in the HI observations are relatively high. We study these in Section 4. First we examine the possibility of measuring the $\delta_{\text{HI}} \times \delta_g$ and $\delta_{\text{HI}} \times \kappa_g$ correlations using MeerKAT and DES. We then study the $\delta_g \times \kappa_{\text{IM}}$ correlation with LSST and MeerKAT/SKA1. Finally, we investigate $\kappa_g \times \kappa_{\text{IM}}$ with LSST and SKA1.

There are exciting prospects for performing clustering and lensing measurements with the forthcoming intensity mapping and optical surveys. The signal-to-noise for many of the cross and auto-spectra we consider is high, so significant progress will occur in the near future, exploiting SKA pathfinders and near-term optical galaxy surveys. The primary goal of our work is to show that it is possible to perform high precision clustering and lensing studies in three dimensions using the intensity mapping technique. We can use these measurements to calibrate the neutral gas density Ω_{HI} , the HI bias parameter b_{HI} and the galaxy-HI correlation coefficient $r_{\text{HI-g}}$. Forecasted constraints on the HI parameters and other cosmological parameters using such measurements will be the subject of future work.

2 THE SURVEYS

2.1 HI intensity mapping

We consider a range of HI surveys, focussing on the SKA and its pathfinder MeerKAT. There are two different observing modes we can consider, namely the single-dish mode and the interferometer mode (see Bull et al. (2015) for details). Below we describe the noise properties for both modes.

2.1.1 Single-dish mode

MeerKAT is a 64-dish SKA pathfinder on the planned site of SKA1-Mid and it will start observing in 2016 with at least 16 dishes. From here onwards, we will refer to its first phase as MeerKAT-16, and its full phase as MeerKAT. The dishes have 13.5 m diameter with number of beams $N_{\text{beams}} = 1$; the redshift range is $0 < z < 1.45$ for the 21cm line and the frequency resolution $\Delta f = 50$ kHz. The system temperature is taken to be $T_{\text{sys}} = 25$ K. The sky area and total observing time are determined by the survey strategy. We will consider two strategies: First, we assume a sky area $A_{\text{sky}} = 1000 \text{ deg}^2$ and a total observation time of 3 weeks, and then we repeat the calculation with $A_{\text{sky}} = 5000 \text{ deg}^2$ and a total observation time of 15 weeks.

The noise properties of such measurements have been described in various works (see, for example, Battye et al. (2013)) and depend on the instrumental noise in a given pixel, its volume and the instrumental response, modelled by the window function $W(k)$. Because the frequency resolution in such surveys is very good (of the order of tens of kHz) we can ignore the instrument response function in the radial direction. However, there is a window function related to the finite angular resolution:

$$W^2(k) = \exp \left[-k^2 \chi(z)^2 \left(\frac{\theta_B}{\sqrt{8 \ln 2}} \right)^2 \right], \quad (1)$$

where $\chi(z)$ is the comoving radial distance at redshift z and $\theta_B \sim \lambda/D_{\text{dish}}$ the beam FWHM of a single dish with diameter D_{dish} at wavelength λ . Considering a redshift bin with limits z_{min} and z_{max} , the survey volume will be given by

$$V_{\text{sur}} = \Omega_{\text{tot}} \int_{z_{\text{min}}}^{z_{\text{max}}} dz \frac{dV}{dz d\Omega} = \Omega_{\text{tot}} \int_{z_{\text{min}}}^{z_{\text{max}}} dz \frac{c\chi(z)^2}{H(z)}, \quad (2)$$

and $\Omega_{\text{tot}} = A_{\text{sky}}$, the sky area the survey scans. The pixel's volume V_{pix} is also calculated from Eq. (2), but with

$$\Omega_{\text{pix}} \simeq 1.13\theta_B^2, \quad (3)$$

and the corresponding pixel z -limits corresponding to the channel width Δf . Finally, the pixel noise σ_{pix} is given by

$$\sigma_{\text{pix}} = \frac{T_{\text{sys}}}{\sqrt{\Delta f t_{\text{total}} (\Omega_{\text{pix}}/\Omega_{\text{tot}}) N_{\text{dishes}} N_{\text{beams}}}}. \quad (4)$$

The MeerKAT radio telescope is a precursor to the SKA telescope and will be integrated into the mid-frequency component of SKA1 (SKA1-Mid). As we will see below, MeerKAT can also be used as an interferometer in its own right.

2.1.2 Interferometer mode

The thermal noise power spectrum for an interferometer array is given by

$$C_{\ell}^{\text{N}} = \frac{(2\pi)^2 T_{\text{sys}}^2}{B t_u d^2 \ell}, \quad (5)$$

where B is the total bandwidth of the observation, t_u is the time each visibility is observed, and ℓ is related to the Fourier wavenumber u by $\ell = 2\pi u$. The observation time t_u is given by (Zaldarriaga et al. 2004; Mao et al. 2008)

$$t_u = \frac{A_{\text{dish}}}{\lambda^2} t_0 n(u), \quad (6)$$

where A_{dish} is the area of an individual dish, t_0 is the total observation time and $n(u)$ -or, equivalently, $n(\ell)$ - is the number density of baselines. Using the above we finally get

$$C_{\ell}^{\text{N}} = \frac{T_{\text{sys}}^2 [\text{FOV}]^2}{B t_0 n(\ell)}, \quad (7)$$

with $1/\text{FOV} \equiv A_{\text{dish}}/\lambda^2 = d^2 u$ (where FOV is the field of view, and λ is the observing wavelength). The required $n(\ell)$ distributions to calculate the noise of SKA1-Mid and MeerKAT in interferometer mode are taken from Bull et al. (2015). The system temperature T_{sys} is the sum of the sky and receiver noise and is given by (Dewdney 2013)

$$T_{\text{sys}} = 28 + 66 \left(\frac{\nu}{300 \text{ MHz}} \right)^{-2.55} \text{ K}, \quad (8)$$

with ν the observing frequency.

The thermal noise of the interferometer is part of the lensing reconstruction noise using the lensing estimator developed in Pourtsidou & Metcalf (2015). In that work the method of 21cm intensity mapping was used to study gravitational lensing over a wide range of post-reionization redshifts — this extends weak lensing measurements to higher redshifts than are accessible with conventional galaxy surveys. Detecting κ with this method would be an important science achievement of the intensity mapping technique.

Central to this detection is understanding $N_{\kappa}(\ell)$,

the lensing reconstruction noise using the aforementioned method. The expression for $N_\kappa(\ell)$ is rather lengthy, so we will not include it here, but the interested reader is referred to Pourtsidou & Metcalf (2015), Appendix C. To summarise, the lensing reconstruction noise involves the underlying dark matter power spectrum $P_{\delta\delta}$, the HI density $\Omega_{\text{HI}}(z)$ as well as the HI mass (or luminosity) moments up to 4th order and, as already stated, the thermal noise of the instrument C_ℓ^N . Note that in the following we will assume an observation (HI source) redshift $z_s = 1.4$ corresponding to a frequency of 592 MHz, bandwidth $B = 40$ MHz corresponding to $\Delta z \sim 0.15$, total observation time $t_0 = 4,000$ hrs and sky area $A_{\text{sky}} = 25,000 \text{ deg}^2$ when we consider MeerKAT and SKA1 in interferometer mode. We remind the reader that the redshift range for MeerKAT is $0 < z < 1.45$, while for SKA1-Mid $0.35 < z < 3.06$ (Band 1).

2.2 Optical galaxy surveys

We consider two photometric surveys: the ongoing Dark Energy Survey (DES) and the planned Large Synoptic Survey Telescope (LSST). DES aims to investigate the nature of the cosmic acceleration and combines four probes of Dark Energy, namely Type Ia Supernovae, Baryonic Acoustic Oscillations (BAOs), galaxy clusters and weak gravitational lensing. LSST is a ground based, wide field survey telescope. One of its main goals is to provide multiple probes of dark energy, with the two most powerful being weak gravitational lens tomography and BAOs.

The DES survey parameters are (Becker et al. 2015) $A_{\text{sky}} = 5000 \text{ deg}^2$, number density of galaxies $n_g = 10 \text{ arcmin}^{-2}$, redshift range $0 < z < 2$ with median redshift $z_0 = 0.7$. We model the redshift distribution of galaxies as

$$\frac{dn}{dz} \propto z^2 \exp[-(z/z_0)^{3/2}]. \quad (9)$$

The LSST survey parameters are assumed to be $f_{\text{sky}} = 0.5$, number density of galaxies $n_g = 40 \text{ arcmin}^{-2}$, redshift range $0 < z < 2$ with median redshift $z_0 = 1$ (Abell et al. 2009).

For these surveys, the primary noise for density measurements arises from shot noise, with the shot noise contribution given by

$$P^{\text{shot}} = \frac{1}{(N_g/V_{\text{sur}})}, \quad (10)$$

with N_g the number of galaxies within the redshift bin under consideration.

These optical surveys can constrain weak lensing via shear measurements. The noise associated with the estimated weak lensing convergence is given by $\sigma_\kappa^2/\bar{n}_b$, where σ_κ is the shape noise of each background galaxy and \bar{n}_b is the number density of background galaxies in the chosen source bin. In the following we assume $\sigma_\kappa = 0.3$.

3 HI ALONE

In this Section we investigate auto-correlations of the HI observables, and we show that high signal-to-noise HI detection can be achieved with near-future facilities like MeerKAT-16, hence there are very good prospects for testing and using the intensity mapping method very soon. Lensing of 21cm sources using the intensity mapping method requires more

powerful instruments like the SKA, and heavily depends on the HI density evolution with cosmic time.

3.1 $\delta_{\text{HI}} \times \delta_{\text{HI}}$ with MeerKAT-16

The detection of HI in autocorrelation using the intensity mapping method is the primary science goal of an intensity mapping instrument. The power spectrum of the HI fluctuations, δ_{HI} , is assumed to take the form

$$P_{\text{HI}}(k, z) = \bar{T}(z)^2 b_{\text{HI}}(z)^2 P_{\delta\delta}(k, z), \quad (11)$$

where $P_{\delta\delta}$ is the underlying dark matter density power spectrum and b_{HI} the HI bias. The mean HI brightness temperature at redshift z is given by (Battye et al. 2013)

$$\bar{T}(z) = 180 \Omega_{\text{HI}}(z) h \frac{(1+z)^2}{H(z)/H_0} \text{ mK}. \quad (12)$$

For our forecasts here and in the next Sections we will use $b_{\text{HI}}(z)$ from Camera et al. (2013) and assume

$$\Omega_{\text{HI}}(z) = 4 \times 10^{-4} (1+z)^{0.6} \quad (13)$$

which has been suggested in Crighton et al. (2015). We also use the fitting formula by Smith et al. (2003) for the non-linear power spectrum.

The error on a power spectrum measurement averaged over a radial bin in k -space of width Δk is (Battye et al. 2013)

$$\delta P_{\text{HI}} = \sqrt{2 \frac{(2\pi)^3}{V_{\text{sur}}} \frac{1}{4\pi k^2 \Delta k} [P_{\text{HI}} + \sigma_{\text{pix}}^2 V_{\text{pix}} W^{-2}]}, \quad (14)$$

where the pixel noise, pixel volume and response window function were described in the previous Section.

The results for HI detection in autocorrelation at a central redshift $z_c = 0.1$ with a redshift bin width $\Delta z = 0.2$ using MeerKAT-16 and the two aforementioned survey strategies (three weeks and $A_{\text{sky}} = 1000 \text{ deg}^2$, fifteen weeks and $A_{\text{sky}} = 5000 \text{ deg}^2$) are shown in Fig. 1, using $\Delta k = 0.01 \text{ Mpc}^{-1}$. We plot the cumulative signal-to-noise ratio (S/N), defined as

$$\frac{S}{N} = \sqrt{\sum_k \left(\frac{P_{\text{HI}}}{\delta P_{\text{HI}}} \right)^2}. \quad (15)$$

As can be seen, these measurements are very precise across a wide range of scales and we can use them to calibrate the combination $\Omega_{\text{HI}} b_{\text{HI}}$. Note that since MeerKAT will cover a wide redshift range $0 < z < 1.45$, we can use tomography to probe the combination $\Omega_{\text{HI}} b_{\text{HI}}$ at different redshifts.

3.2 $\kappa_{\text{IM}} \times \kappa_{\text{IM}}$ with MeerKAT/SKA1

The lensing convergence power spectrum from sources at redshift z_s is given by the expression

$$C_{\kappa\kappa}(\ell) = \frac{9\Omega_m^2 H_0^3}{4c^3} \int_0^{z_s} dz \frac{P_{\delta\delta}(k = \ell/\chi, z)}{a^2 H(z)/H_0} \left[\frac{\hat{\chi}_s - \chi}{\hat{\chi}_s} \right]^2, \quad (16)$$

with $\hat{\chi}_s \equiv \chi(z_s)$. The error in the measurement of the power spectrum is

$$\delta C_{\kappa\kappa}(\ell) = \sqrt{\frac{2}{(2\ell+1)\Delta\ell f_{\text{sky}}} (C_{\kappa\kappa}(\ell) + N_\kappa(\ell))}, \quad (17)$$

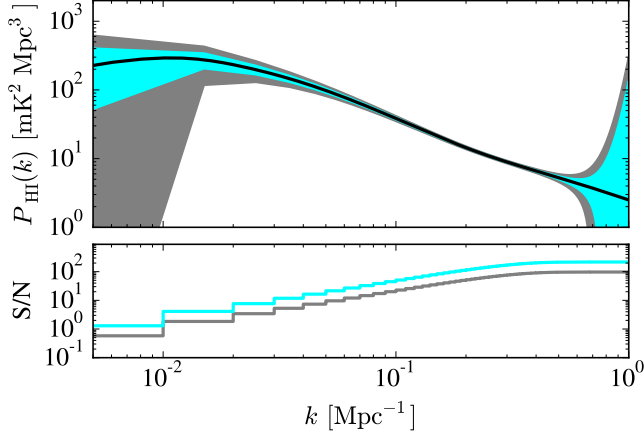


Figure 1. HI detection in autocorrelation with MeerKAT-16. The black solid line is the predicted power spectrum $P_{\text{HI}}(k, z_c)$ at $z_c = 0.1$. The grey area represents the measurement errors δP_{HI} taking $A_{\text{sky}} = 1000 \text{ deg}^2$ and a total observation time of 3 weeks, while the cyan area corresponds to $A_{\text{sky}} = 5000 \text{ deg}^2$ and a total observation time of 15 weeks. The cumulative signal-to-noise (S/N) defined in Eq. (15) is also shown.

where $N_\kappa(\ell)$ is the lensing reconstruction noise using the intensity mapping method described in the previous Section.

In Pourtsidou & Metcalf (2015) it was found that the signal-to-noise is strongly dependent on the possible evolution of the HI mass function. More specifically, it was shown that assuming the no-evolution scenario (which is the most conservative, but also less realistic approach), precise measurements can only be made with an SKA2-like instrument; however assuming instead a model where the HI density $\Omega_{\text{HI}}(z)$ increases by a factor of 5 by redshift $z = 3$ and then slowly decreases towards redshift $z = 5$, as suggested by the DLA observations from Peroux et al. (2003), high signal-to-noise can be achieved even with SKA1.

In this work we instead use the HI evolution model given by Eq. (13), which fits observations in a wide redshift range, and we implement this evolution in the ϕ^* parameter of the HI mass function which is locally measured by the HIPASS survey (Zwaan et al. 2003). We also note that in Pourtsidou & Metcalf (2015) the telescope distribution within the array was approximated as uniform for the calculation of the thermal noise component, while here we use the baseline designs from Bull et al. (2015). In Fig. 2 we show results for MeerKAT and SKA1 assuming HI sources are at $z_s = 1.4$ and using $\Delta\ell = 50$.

As we can see, we can detect lensing using the intensity mapping method and SKA1, but using MeerKAT detection in autocorrelation is not possible. However, below we will demonstrate that cross-correlations can enhance the signal-to-noise of the lensing measurements.

3.3 $\delta_{\text{HI}} \times \kappa_{\text{IM}}$ with MeerKAT/SKA1

We are going to examine the correlation of a foreground (f) density tracer field with the background (b) convergence κ field, where both are probed by the IM survey.

Using the Limber approximation (Limber 1954) the an-

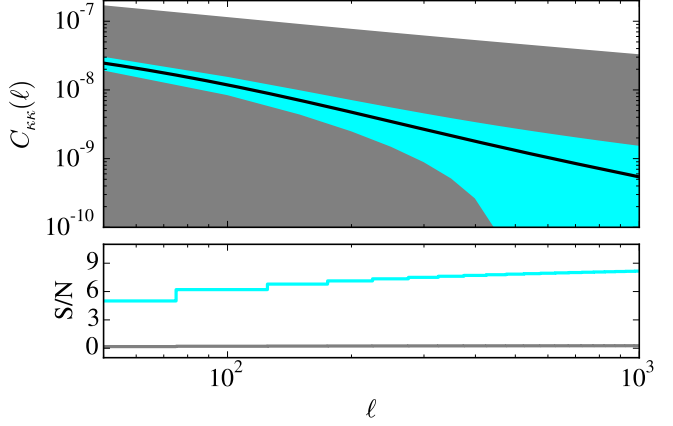


Figure 2. The convergence power spectrum and measurement errors with MeerKAT (grey) and SKA1 (cyan), using the intensity mapping method, together with the cumulative signal-to-noise (S/N) ratio. Sources are at $z_s = 1.4$.

gular cross-power spectrum $C_{\text{HI}\kappa}$ is given by

$$C_{\text{HI}\kappa}(\ell) = \frac{3\Omega_m H_0^2}{2c^2} \int \frac{d\chi_f}{a(\chi_f)} W_f(\chi_f) \int d\chi_b W_b(\chi_b) \times \frac{\chi_b - \chi_f}{\chi_b \chi_f} \bar{T}(\chi_f) r_{\text{HI}} b_{\text{HI}}(\chi_f) P_{\delta\delta} \left(\frac{\ell}{\chi_f}, \chi_f \right), \quad (18)$$

where χ is the comoving distance, W_f (W_b) the foreground (background) redshift distribution and r_{HI} is a correlation coefficient quantifying the potential stochasticity between the dark matter density and the HI density fields. If the foreground lens slice is narrow enough in redshift ($\Delta z \sim 0.1$ is sufficient), we can approximate the foreground redshift distribution as a delta function at a distance $\hat{\chi}_f$, $W_f(\chi_f) = \delta^D(\chi_f - \hat{\chi}_f)$. We also use the delta function approximation at a distance $\hat{\chi}_b$ for the distribution of the 21cm sources. We then find

$$C_{\text{HI}\kappa}(\ell) = \frac{3\Omega_m H_0^2}{2c^2} \left(\frac{\bar{T}(\hat{\chi}_f) r_{\text{HI}} b_{\text{HI}}(\hat{\chi}_f) P_{\delta\delta} \left(\frac{\ell}{\hat{\chi}_f}, \hat{\chi}_f \right)}{a(\hat{\chi}_f) \hat{\chi}_f} \right) \frac{\chi_b - \hat{\chi}_f}{\chi_b}.$$

It is useful to translate the HI power into multipole space,

$$C_{\text{HI-HI}}(\ell) = \int dz E(z) W^2(z) [\bar{T}(z)]^2 P_{\delta\delta}(\ell/\chi(z), z) / \chi^2(z), \quad (19)$$

with $W(z)$ a projection kernel which we take to be a top-hat function equal to $1/\Delta z$ within the redshift bin and 0 otherwise.

The error in the cross correlation, for a bin of width $\Delta\ell$ and for a survey scanning a fraction of the sky f_{sky} , is

$$\delta C_{\text{HI}\kappa}(\ell) = \sqrt{\frac{2}{(2\ell+1)\Delta\ell f_{\text{sky}}}} \times \sqrt{C_{\text{HI}\kappa}^2(\ell) + (C_{\text{HI-HI}}(\ell) + N(\ell)) (C_{\kappa\kappa}(\ell) + N_\kappa(\ell))}, \quad (20)$$

with $N_\kappa(\ell)$ from Pourtsidou & Metcalf (2014, 2015). For the single-dish mode, the noise term $N(\ell)$ is given by (Battye et al. 2013)

$$N(\ell) = \Omega_{\text{pix}} (\sigma_{\text{pix}})^2 \exp[\ell(\ell+1)(\theta_B/\sqrt{8\ln 2})^2], \quad (21)$$

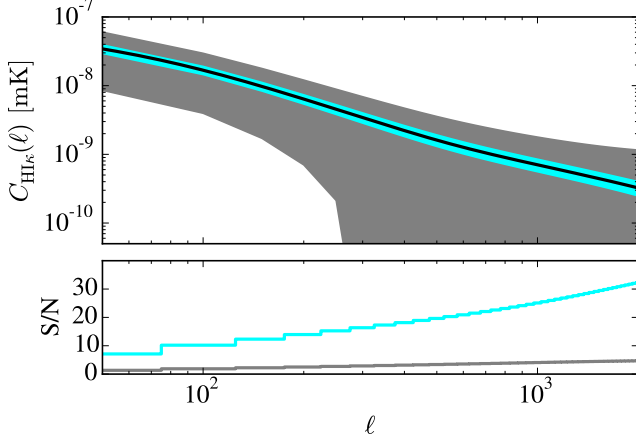


Figure 3. The $C_{\text{HI}\kappa}$ cross correlation power spectrum and measurement errors with MeerKAT (grey) and SKA1 (cyan), together with the cumulative signal-to-noise (S/N) ratio.

with $\sigma_{\text{pix}} = T_{\text{sys}}/\sqrt{2\Delta f t_{\text{obs}}}$. For the interferometer mode, $N(\ell) = C_{\ell}^N$, defined in Eq. (7).

The results are shown in Fig. 3 assuming the MeerKAT and SKA1 parameters in interferometer mode. The foreground central redshift is $z_c = 0.5$ with $\Delta z = 0.1$. We see that using MeerKAT in interferometer mode we have the possibility of detecting the lensing convergence in cross correlation with the HI density using the intensity mapping method (with a cumulative S/N ~ 5). With SKA1 we can achieve a high signal-to-noise detection. Using tomography (for example, taking different foreground bins z_c) we can perform measurements with a similar signal-to-noise level along redshift.

4 CROSS-CORRELATING WITH GALAXY SURVEYS

As we saw above, the prospects for detecting the HI density fluctuations are very good even for a near-term instrument such as MeerKAT-16; however, the measurement of convergence with HI intensity mapping might require an advanced SKA measurement. We also showed that cross-correlating the density and convergence using an IM survey can greatly improve the signal-to-noise for the lensing detection. It is interesting to examine to what extent the HI detections could be accelerated by cross-correlating these measurements with density and convergence derived from galaxy surveys, where the noise and potential systematics are expected to be independent.

For the purposes of these projections we assume that the galaxy power spectrum is related to the density by $P_{gg}(k, z) = b_g^2 P_{\delta\delta}(k, z)$ and assume the galaxy bias $b_g(z)$ evolves as $\sqrt{1+z}$. In addition, there is potential stochasticity between the dark matter density and the galaxy density fields; this is quantified by the correlation coefficient r_g .

4.1 $\delta_{\text{HI}} \times \delta_g$ with MeerKAT-16 and DES

The $\delta_{\text{HI}} \times \delta_g$ combination, i.e. the cross-correlation between a 21cm intensity map with large-scale structure traced by

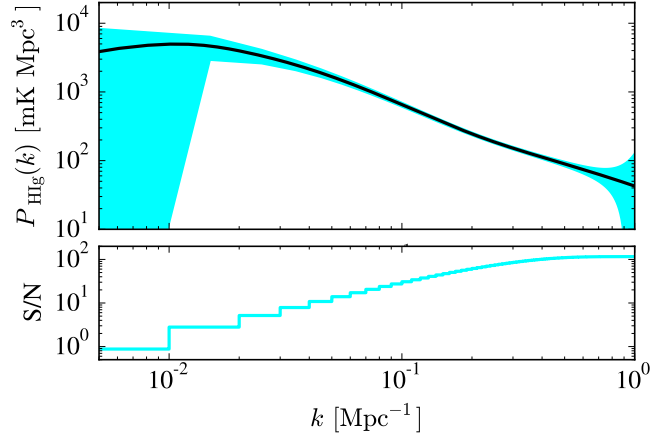


Figure 4. The $P_{\text{HI},g}$ cross correlation power spectrum and measurement errors with MeerKAT-16 and DES, together with the cumulative signal-to-noise (S/N) ratio. Note $t_{\text{total}} = 1$ week for MeerKAT-16.

galaxies has been investigated previously (Chang et al. 2010; Masui et al. 2013) at redshift $z \sim 1$. This correlation constrains $\Omega_{\text{HI}} b_{\text{HI}} r_{\text{HI-g}}$. For this cross-correlation power spectrum

$$P_{\text{HI},g}(k) = \bar{T} b_{\text{HI}} b_g r_{\text{HI-g}} P_{\delta\delta}(k), \quad (22)$$

the error averaged over a radial bin in k -space of width Δk is

$$\delta P_{\text{HI},g} = \sqrt{2 \frac{(2\pi)^3}{V_{\text{sur}}} \frac{1}{4\pi k^2 \Delta k} \times P_{\text{HI},g}^2 + (P_{\text{HI}} + \sigma_{\text{pix}}^2 V_{\text{pix}} W^{-2})(P_{gg} + P^{\text{shot}})}, \quad (23)$$

where the HI noise and shot noise terms were defined above.

For our forecasts here we will set $r_{\text{HI-g}} = 1$ for simplicity. We will assume MeerKAT-16 measurements with $A_{\text{sky}} = 5000 \text{ deg}^2$ and a total observing time of 1 week for this case, and combine it with DES. The redshift bin we use is $0 < z < 0.2$ with central redshift $z_c = 0.1$. As we can see from Fig. 4, these measurements are very precise across a wide range of scales even if a single week's observing time is used.

We will also be able to perform tomographic studies across the redshift range $0 < z < 1.45$, constraining the $\Omega_{\text{HI}} b_{\text{HI}} r_{\text{HI-g}}$ combination as a function of redshift.

4.2 $\delta_{\text{HI}} \times \kappa_g$ with MeerKAT and DES

We are now going to examine the cross correlation of the HI density fluctuations with the lensing convergence using a galaxy survey.

The formulae used for the signal and error calculations are the same as in the $\delta_{\text{HI}} \times \kappa_{\text{IM}}$ case but instead of the IM lensing reconstruction noise $N_{\kappa}(\ell)$ we have the galaxy survey shape noise $\sigma_{\kappa}^2/\bar{n}_b$.

For DES lensing measurements, we assume a source bin with $z_b = 1.5$ and width $\Delta z = 1.0$ and $\sigma_{\kappa} = 0.3$, while for MeerKAT we use a bin with central redshift $z_c = 0.1$ and width $\Delta z \simeq 0.08$ (equivalently, $\Delta f = 100 \text{ MHz}$), with $t_{\text{total}} = 15$ weeks. We also take $A_{\text{sky}} = 5000 \text{ deg}^2$ and $\Delta \ell = 50$. The results for MeerKAT-16 are shown in Fig. 5 — note

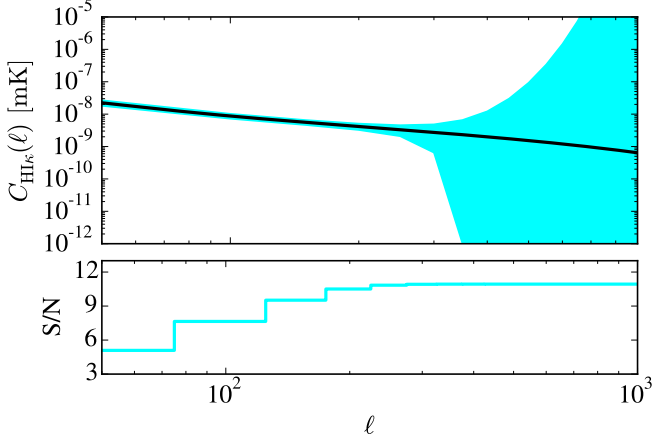


Figure 5. The $C_{\text{HI}\kappa}$ cross correlation power spectrum and measurement errors with MeerKAT-16 and DES, together with the cumulative signal-to-noise (S/N) ratio.

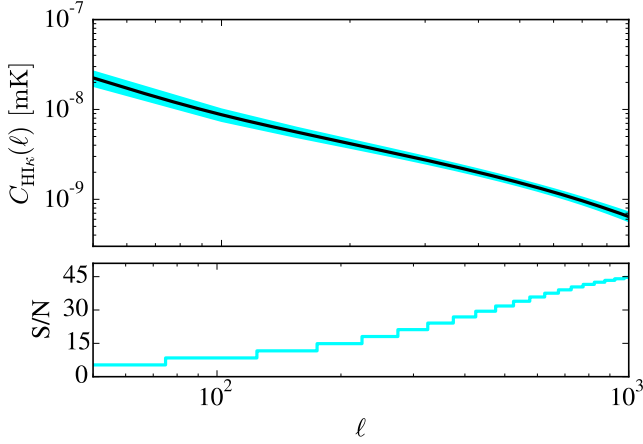


Figure 6. The $C_{\text{HI}\kappa}$ cross correlation power spectrum and measurement errors with MeerKAT (in interferometer mode) and DES, together with the cumulative signal-to-noise (S/N) ratio.

that the dominant noise term is from the HI noise $N(\ell)$ defined in Eq. (21) which diverges as we reach the limits set by the beam resolution.

In Fig. 6 we show the results for the full MeerKAT, instead in interferometer mode. One can see that this mode allows smaller scales to be probed with significant signal-to-noise. These measurements can constrain the $\Omega_{\text{HI}} b_{\text{HI}} r_{\text{HI}}$ combination. Using tomography this can be achieved across a wide range of redshift, which is very important as there is currently a lot of uncertainty regarding the HI evolution with cosmic time.

4.3 $\delta_g \times \kappa_{\text{IM}}$ with LSST and MeerKAT/SKA1

A very interesting combination to consider is the cross-correlation of the galaxy density field with the lensing convergence probed via the intensity mapping method. Cross-correlating κ_{IM} with δ_g can help boost the signal-to-noise ratio of the κ detection using the method developed in Pourtsidou & Metcalf (2015) and also remove systematic effects

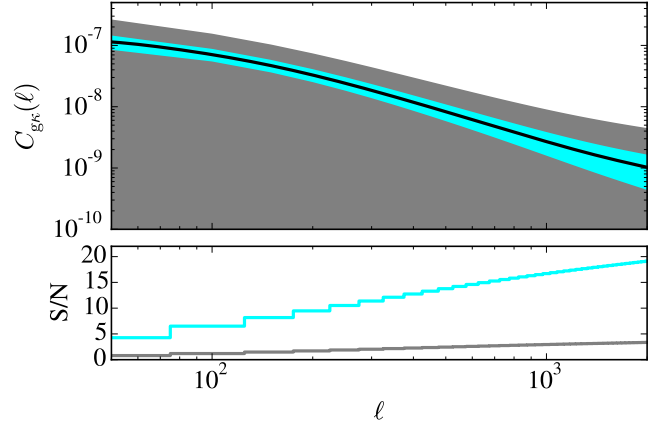


Figure 7. The $C_{g\kappa}$ cross correlation power spectrum and measurement errors with LSST and SKA1 (cyan), and LSST and MeerKAT (grey), together with the cumulative signal-to-noise (S/N) ratio.

since optical and intensity mapping surveys use completely different instruments and strategies. In this case we have

$$C_{g\kappa}(\ell) = \frac{3\Omega_m H_0^2}{2c^2} \left(\frac{r_g b_g(\hat{\chi}_f) P_{\delta\delta}(\frac{\ell}{\hat{\chi}_f}, \hat{\chi}_f)}{a(\hat{\chi}_f)} \right) \frac{\hat{\chi}_s - \hat{\chi}_f}{\hat{\chi}_f \hat{\chi}_s}. \quad (24)$$

The corresponding error is

$$\delta C_{g\kappa}(\ell) = \sqrt{\frac{2}{(2\ell+1)\Delta\ell f_{\text{sky}}}} \times \sqrt{C_{g\kappa}^2(\ell) + \left(C_{g\kappa}(\ell) + \frac{1}{\bar{n}_g}\right)(C_{\kappa\kappa}(\ell) + N_{\kappa}(\ell))}. \quad (25)$$

Here

$$C_{g\kappa}(\ell) = \int dz E(z) W^2(z) P_{\delta\delta}(\ell/\chi(z), z)/\chi^2(z) \quad (26)$$

and \bar{n}_g is the number density of galaxies in the redshift bin under consideration.

We show results in Fig. 7 combining LSST and SKA1, as well as LSST and MeerKAT, with the 21 cm sources at redshift $z_s = 1.4$ and the foreground density tracer field at $z_f = 1.0$ with $\Delta z_f = 0.2$. We use $\Delta\ell = 50$.

We see that a high signal-to-noise detection can be achieved with SKA1 in combination with an optical survey like LSST. Comparing with the results presented in Fig. 3, we see that the $\delta_{\text{HI}} \times \kappa_{\text{IM}}$ cross-correlation is more powerful; however, the $\delta_g \times \kappa_{\text{IM}}$ correlation we considered here is less prone to systematic effects.

4.4 $\kappa_g \times \kappa_{\text{IM}}$ with LSST and MeerKAT/SKA1

Finally, we cross-correlate the lensing convergence κ_g measured with LSST from sources within our chosen bin centred at $z_b = 1$, and κ_{IM} measured with the MeerKAT/SKA1 instruments assuming 21 cm sources at $z_s = 1.4$. The results are shown in Fig. 8. We have used $\Delta\ell = 50$.

We see that, in combination with a powerful optical galaxy survey like LSST, both MeerKAT and Phase 1 of the SKA can achieve detection of the lensing convergence

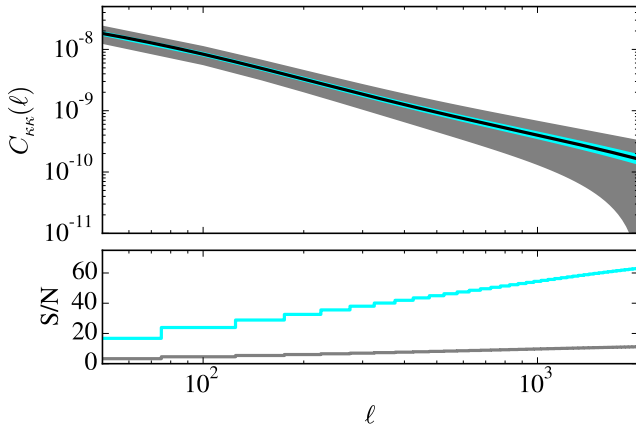


Figure 8. The $C_{\kappa\kappa}$ cross correlation power spectrum and measurement errors with LSST and SKA1 (cyan), and LSST and MeerKAT (grey), together with the cumulative signal-to-noise (S/N) ratio.

coming from 21cm sources with a high signal-to-noise. This combination could also alleviate issues arising from systematic effects.

Furthermore, as shown in (Pourtsidou & Metcalf 2015), Phase 2 of the SKA (SKA2) can provide high precision measurements of κ (in auto correlation) at redshifts $z \sim 2 - 3$. This means that we can use tomographic studies along many redshift bins in order to map the evolution of the growth function at redshifts higher than those of galaxy shear surveys. This will be the subject of future work.

5 DISCUSSION AND CONCLUSIONS

In this paper, we have shown how ongoing and future intensity mapping surveys and optical galaxy surveys can be used to perform high precision clustering and lensing measurements. We considered a range of HI surveys, concentrating on the performance of the MeerKAT SKA pathfinder, as well as the full SKA Phase 1, and the DES and LSST optical galaxy surveys.

Our auto correlation forecasts show that high signal-to-noise HI detection can be achieved already with the first phase of MeerKAT, MeerKAT-16. This is very important for testing the intensity mapping method and calibrating the HI evolution across redshift using tomographic measurements from MeerKAT and Phase 1 of the SKA.

The measurement of the lensing convergence in auto correlation is much more demanding and heavily depends on the unknown evolution of the HI density (Pourtsidou & Metcalf 2015). Our cross correlation studies show that using the HI or galaxy density fields in cross correlation with κ_{IM} considerably improves the 21cm lensing detection prospects. The same is true when using κ_g in cross correlation with κ_{IM} . Cross-correlating the galaxy and HI densities will also give us information about the galaxy-HI correlation coefficient. A significant advantage of cross correlating HI intensity mapping and optical galaxy surveys is the alleviation of the issues arising from systematic effects.

The prospects of detecting -for the first time- HI clustering and lensing of 21cm emission using the intensity map-

ping technique with the MeerKAT pathfinder are particularly exciting. HI can be detected with high signal-to-noise with MeerKAT-16, which is expected to be commissioned in 2016. Using the full MeerKAT instrument in interferometer mode -expected 2017/18- we have the possibility of detecting 21cm lensing using IM. This will be an important science achievement of the method and will give us valuable information on how to exploit it for higher redshifts using SKA1.

Finally, we note that in future work we plan to extend these studies to include forecasted constraints on the HI density Ω_{HI} , the HI bias b_{HI} , the galaxy-HI correlation coefficient $r_{\text{HI-g}}$ and other cosmological parameters.

6 ACKNOWLEDGMENTS

This work was supported by STFC grant ST/H002774/1. RBM's work is part of the project GLENCO, funded under the Seventh Framework Programme, Ideas, Grant Agreement n. 259349. The authors would like to thank Philip Bull, Stefano Camera, Roy Maartens and Mario Santos for useful discussions and feedback.

REFERENCES

- Abell P. A., et al., 2009
- Ansari R., Campagne J., Colom P., Goff J. L., Magneville C., et al., 2012, *Astron.Astrophys.*, 540, A129
- Battye R., Browne I., Dickinson C., Heron G., Maffei B., et al., 2013, *Mon. Not. Roy. Astron. Soc.*, 434, 1239
- Battye R. A., Davies R. D., Weller J., 2004, *Mon.Not.Roy.Astron.Soc.*, 355, 1339
- Becker M. R., et al., 2015
- Bull P., Ferreira P. G., Patel P., Santos M. G., 2015, *Astrophys.J.*, 803, 21
- Camera S., Santos M. G., Ferreira P. G., Ferramacho L., 2013, *Phys. Rev. Lett.*, 111, 171302
- Chang T.-C., Pen U.-L., Bandura K., Peterson J. B., 2010, *Nature*, 466, 463
- Chang T.-C., Pen U.-L., Peterson J. B., McDonald P., 2008, *Phys.Rev.Lett.*, 100, 091303
- Crichton N. H. M., et al., 2015
- Dewdney P., 2013, *SKA Project Documents*, pp 1–98
- Limber D. N., 1954, *Astrophys.J.*, 119, 655
- Loeb A., Wyithe S., 2008, *Phys.Rev.Lett.*, 100, 161301
- Mao Y., Tegmark M., McQuinn M., Zaldarriaga M., Zahn O., 2008, *Phys.Rev.*, D78, 023529
- Masui K., Switzer E., Banavar N., Bandura K., Blake C., et al., 2013, *Astrophys.J.*, 763, L20
- Peroux C., McMahon R. G., Storrie-Lombardi L. J., Irwin M. J., 2003, *Mon.Not.Roy.Astron.Soc.*, 346, 1103
- Peterson J. B., Aleksan R., Ansari R., Bandura K., Bond D., et al., 2009
- Pourtsidou A., Metcalf R. B., 2014, *Mon.Not.Roy.Astron.Soc.*, 439, L36
- Pourtsidou A., Metcalf R. B., 2015, *Mon.Not.Roy.Astron.Soc.*, 448, 2
- Santos M. G., Bull P., Alonso D., Camera S., Ferreira P. G., et al., 2015
- Seo H.-J., Dodelson S., Marriner J., McGinnis D., Stebbins A., et al., 2010, *Astrophys.J.*, 721, 164

- Smith R., et al., 2003, Mon.Not.Roy.Astron.Soc., 341, 1311
Switzer E., Masui K., Bandura K., Calin L. M., Chang
T. C., et al., 2013, Mon.Not.Roy.Astron.Soc., 434, L46
Zaldarriaga M., Furlanetto S. R., Hernquist L., 2004, As-
trophys. J., 608, 622
Zwaan M. A., et al., 2003, Astron.J., 125, 2842